Energy and AI 1 (2020) 100003

Contents lists available at ScienceDirect

Energy and AI

journal homepage: www.elsevier.com/locate/egyai

Towards online optimisation of solid oxide fuel cell performance: Combining deep learning with multi-physics simulation

Haoran Xu[a,1], Jingbo Ma[b,1], Peng Tan[c], Bin Chen[d], Zhen Wu[e], Yanxiang Zhang[b], Huizhi Wang[f], Jin Xuan[a,*], Meng Ni[g,h,*]

[a] Department of Chemical Engineering, Loughborough University, Loughborough, United Kingdom
[b] National Key Laboratory for Precision Hot Processing of Metals, School of Materials Science and Engineering, Harbin Institute of Technology, Harbin 150001, Heilongjiang, China
[c] Department of Thermal Science and Energy Engineering, University of Science and Technology of China, Hefei 230026, China
[d] Institute of Deep Earth Sciences and Green Energy, Shenzhen University, Shenzhen 518060, China
[e] Shaanxi Key Laboratory of Energy Chemical Process Intensification, School of Chemical Engineering and Technology, Xi'an Jiaotong University, Xi'an, China
[f] Department of Mechanical Engineering, Imperial College London, London SW7 2AZ United Kingdom
[g] Department of Building and Real Estate, Building Energy Research Group, The Hong Kong Polytechnic University, Hung Hom, Kowloon, Hong Kong, China
[h] Environmental Energy Research Group, Research Institute for Sustainable Urban Development (RISUD), The Hong Kong Polytechnic University, Hung Hom, Kowloon, Hong Kong, China

HIGHLIGHTS

- A hybrid model is developed for SOFCs combining MPS and deep learning algorithm.
- A detailed study is conducted considering the fuel complexity and thermal effects.
- The deep learning algorithm is well trained for prediction with an accuracy > 99%.
- Online optimisation of SOFC performance is achieved using the genetic algorithm.
- An efficiency > 65% is ensured under safe operation in real-time optimisation.

GRAPHICAL ABSTRACT

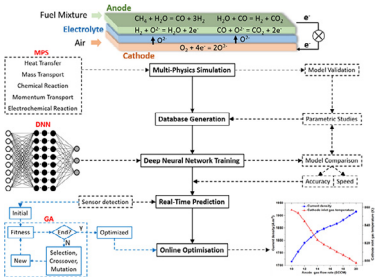

ARTICLE INFO

Article history:
Received 28 February 2020
Received in revised form 27 March 2020
Accepted 27 March 2020
Available online 19 April 2020

Keywords:
Solid oxide fuel cell
Multi-physics simulation
Artificial intelligence
Deep neural network
Hybrid model
On-line optimisation

ABSTRACT

The use of solid oxide fuel cells (SOFCs) is a promising approach towards achieving sustainable electricity production from fuel. The utilisation of the hydrocarbons and biomass in SOFCs is particularly attractive owing to their wide distribution, high energy density, and low price. The long-term operation of SOFCs using such fuels remains difficult owing to a lack of an effective diagnosis and optimisation system, which requires not only a precise analysis but also a fast response. In this study, we developed a hybrid model for an on-line analysis of SOFCs at the cell level. The model combines a multi-physics simulation (MPS) and deep learning, overcoming the complexity of MPS for a model-based control system, and reducing the cost of building a database (compared with the experiments) for the training of a deep neural network. The maximum temperature gradient and heat generation are two target parameters for an efficient operation of SOFCs. The results show that a precise prediction can be achieved from a trained AI algorithm, in which the relative error between the MPS and AI models is less than 1%. Moreover, an online optimisation is realised using a genetic algorithm, achieving the maximum power density within the limitations of the temperature gradient and operating conditions. This method can also be applied to the prediction and optimisation of other non-liner, dynamic systems.

* Corresponding authors.
E-mail addresses: J.Xuan@lboro.ac.uk (J. Xuan), meng.ni@polyu.edu.hk (M. Ni).

https://doi.org/10.1016/j.egyai.2020.100003

Nomenclature

DL	Deep learning
DNN	Deep neural network
GA	Genetic algorithm
LSM	Lanthanum strontium manganite
MPS	Multi-physics simulation
SCCM	Standard cubic centime per minute
ScSZ	Scandium stabilized zirconium
SMR	Steam methane reforming
SOFC	Solid oxide fuel cell
TPB	Triple phase boundary
WGSR	Water gas shift reaction

Roman

B_0	Permeability coefficient, m^2
c_{CO_2}	Mole concentration of carbon dioxide, $mol{\cdot}m^{-3}$
c_{H_2O}	Mole concentration of water, $mol{\cdot}m^{-3}$
C_p	Heat capacity at constant pressure
D_i^{eff}	Effective diffusivity of species i, $m^2{\cdot}s^{-1}$
D_{ik}^{eff}	Knudsen diffusion coefficient of i, $m^2{\cdot}s^{-1}$
D_{im}^{eff}	Molecular diffusion coefficient of i, $m^2{\cdot}s^{-1}$
E_{act}	Activation energy, $J{\cdot}mol^{-1}$
E_{CO}	Equilibrium potential for carbon monoxide oxidization, V
E_{CO}^0	Standard equilibrium potential for carbon monoxide oxidization, V
E_{eq}	Equilibrium Nernst potential, V
E_{H_2}	Equilibrium potential for hydrogen oxidization, V
$E_{H_2}^0$	Standard equilibrium potential for hydrogen oxidization, V
F	Faraday constant, 96,485 $C{\cdot}mol^{-1}$
i	Operating current density, $A{\cdot}m^{-2}$
i_o	Exchange current density, $A{\cdot}m^{-2}$
n	Number of electrons transferred per electrochemical reaction
N_i	Flux of mass transport, $kg{\cdot}m^{-3}{\cdot}s^{-1}$
p	(Partial) Pressure, Pa
P_{CO}^L	Local CO partial pressures, Pa
$P_{CO_2}^L$	Local CO_2 partial pressures, Pa
$P_{H_2}^L$	Local H_2 partial pressures, Pa
$P_{H_2O}^L$	Local H_2O partial pressures, Pa
$P_{O_2}^L$	Local O_2 partial pressures, Pa
R	Gas constant, 8.314 $J{\cdot}mol^{-1}{\cdot}K^{-1}$
R_{SMR}	Steam methane reforming reaction
R_{WGSR}	Water gas shift reaction
T	Temperature, K
u	Velocity field, $m^3{\cdot}s^{-1}$
V	Volume fraction
y_i	Mole fraction of component i

Greek letters

α	Charge transfer coefficient
ϵ	Porosity
η_{act}	Activation overpotential loss, V
η_{ohmic}	Ohmic overpotential loss, V
κ	Permeability, m^2
λ	Heat conductivity
μ	Dynamic viscosity of fluid, Pa·s
ρ	Fluid density, $kg{\cdot}m^{-3}$
σ	Conductivity, $S{\cdot}m^{-1}$
γ	Pre-exponential factor, $A\ m^{-2}$
τ	Tortuosity

Subscripts

an	Anode
ca	Cathode
CO	Carbon monoxide
CO_2	Carbon dioxide
el	Electrolyte
H_2	Hydrogen
l	Ionic phase
O_2	Oxygen
s	Electronic phase

Superscripts

0	Parameter at equilibrium conditions
eff	Effective
L	Local

1. Introduction

The growing concerns regarding the sustainable development of human society and the rising risk of ecological crises require significant efforts towards the development of renewable energy conversion and storage technologies [1,2]. Solid oxide fuel cells (SOFCs) achieve a highly efficient electricity generation from fuel [3]. As high-temperature electrochemical devices, SOFCs have a simple structure with the electrolyte sandwiched between porous electrodes. At the applied electrical potential, the fuel and oxygen are electrochemically oxidized and reduced at the anode and cathode, respectively. SOFCs use non-noble catalysts (e.g. nickel) [4], making them economical and robust for various types of fuels, including hydrogen [5], carbon monoxide [6], hydrocarbons [7], coal [8], biomass [9], and even ammonia [10].

The use of hydrocarbons and biomass in SOFCs is especially attractive owing to their low costs, wide availability, and high energy density per volume [11]. However, the composition of such fuels is complex, which causes multiple electrochemical/chemical reactions to occur [12]. This not only results in complex electricity/heat generation processes, it also creates difficulties in predicting and optimising the performance [13]. To ensure a safe and efficient long-term operation of SOFCs, optimised working parameters are required to avoid a thermal failure and other problems, and a model-based control system with a precise analysis and fast response is needed [14].

SOFCs are highly non-linear with various physical/chemical processes. The most widely used method for an SOFC analysis is based on physical conservation laws such as a multi-physics simulation (MPS) [15–17]. An MPS has shown a high accuracy in terms of the performance analysis, but it remains too complex for on-line prediction and optimisation. Compared with the MPS method (which is usually applied in 2D or 3D), a black-box model (BBM, 0D) can be developed with a pair of inputs and outputs [18]. When trained through a proper procedure, a BBM can quickly predict the system performance with the given inputs [19,20]. Using a deep learning (DL) algorithm (such as the deep neural network (DNN) adopted in this study), a BBM has been proven to be effective for non-linear systems [21]. As determined by Arriagada et al. [22], an artificial neural network is capable of predicting the performance of SOFCs with high accuracy. However, a well-trained DL algorithm requires a large database, necessitating a lengthy data collection from the experimental results [23].

Combining an MPS and an AI-based BBM has become an alternative method in the analysis of non-linear, dynamic systems such as SOFCs [23,24]. With a proper validation, an MPS model can generate the amount of data required for the training of a DL algorithm. In addition, an MPS method requires much less time and costs compared with an experimental method. Moreover, an MPS can provide detailed information

[1] These authors contributed equally to this paper.

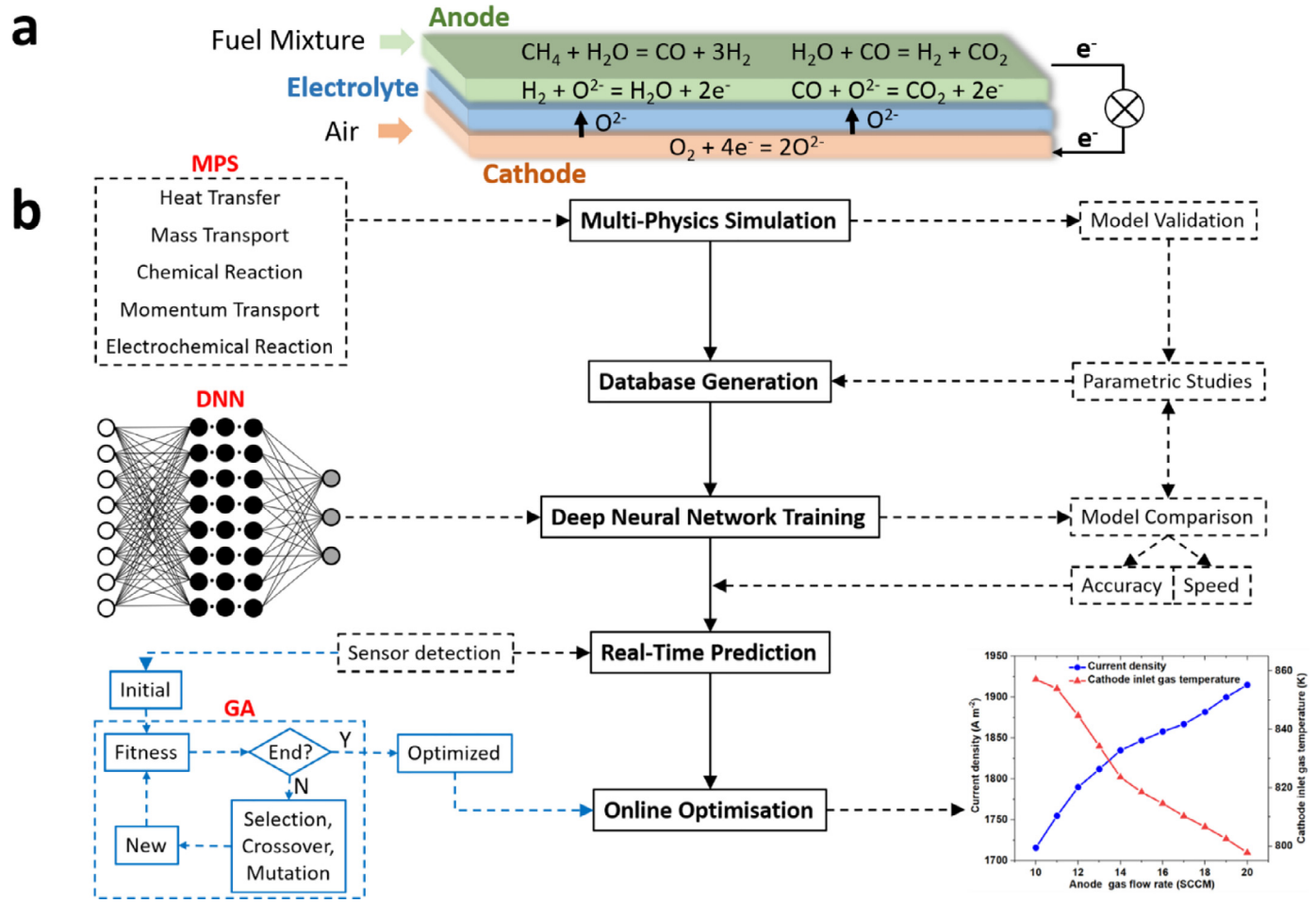

Fig. 1. (a) Schematic of an SOFC with complex fuel composition and (b) the workflow for the development of combined multi-physics model and AI simulation.

of the system under various (or extreme) operating conditions, which is difficult to collect through experiments. Trained using a database developed using an MPS method, the DL algorithm can quickly predict the system performance when given the input parameters, making up for the inadequacy of the MPS in terms of a fast response [25]. With the adoption of a genetic algorithm (GA), an online optimisation of the system regarding the target parameters can be further realised. In this way, the cycle of detection to online analysis and optimisation is closed. Based on this idea, the present paper demonstrates the concept of combining deep learning algorithms with an MPS to predict and optimise the performance of SOFCs with a complex fuel composition.

2. Model development

2.1. Framework for the online prediction and optimisation of SOFC performance

Fig. 1 shows a schematic of an SOFC and the workflow of the proposed scheme. First, the MPS model was developed in accordance with the experimental parameters and validated based on the experimental results. Parametric studies were then conducted to investigate the effects of different parameters on the SOFC performance. Meanwhile, a dataset of the inputs and outputs was generated from multi-physics models. Using this dataset, a DNN was trained to map the relationships among the operating conditions and the performance parameters. New outputs were generated using the DNN model, and the results were compared with those from the MPS model to validate the accuracy. Finally, the trained DNN model was used for optimisation of the SOFC performance through a combination with a GA.

2.2. Development of MPS model for SOFC

The MSP model uses the same geometry and material properties of an SOFC as applied in a previous study [26]. The tubular SOFC has an inner diameter of 8.5 mm, with radial thicknesses of the anode, electrolyte, and cathode of 695, 20, and 15 μm, respectively. The key properties of the SOFC material are listed in Table 1. Processes including chemical/electrochemical reactions, a fluid flow, and a heat transfer are considered using the non-linear solver in COMSOL Multiphysics for the model development. The governing equation and boundary conditions adopted are introduced below.

2.2.1. Electrochemical reaction

With a complex fuel composition (mainly H_2 and CO) at the anode and air at the cathode, the electrochemical reactions of H_2-O_2 and CO-O_2 pairs are considered, as given from Eqs. (1)–(3).

$$H_2 + O^{2-} = H_2O + 2e^- \quad (1)$$

$$CO + O^{2-} = CO_2 + 2e^- \quad (2)$$

$$O_2 + 4e^- = 2O^{2-} \quad (3)$$

The electrons (released at the anode) move towards the cathode through an external circuit, which closes the cycle and generates electricity. At a certain operating current, the corresponding voltage can be calculated as in Eq. (4).

$$V = E_{eq} - \eta_{act} - \eta_{ohmic} \quad (4)$$

Table 1
Properties of the adopted materials [26].

Parameters	Value or expression	Unit
Conductivity		
σ_{ScSZ}	$69,200 \times e^{\frac{-9681}{T}}$	S m^{-1}
σ_{YSZ}	$33,400 \times e^{\frac{-10,300}{T}}$	S m^{-1}
σ_{Ni}	$4.2 \times 10^6 - 1,065.3T$	S m^{-1}
σ_{LSM}	$4.2 \times 10^7 \exp(-1,150/T)$	S m^{-1}
Porosity		
ε_a	0.36	
ε_c	0.36	
Tortuosity		
τ_a	3	
τ_c	3	
Triple Phase Boundary		
S_{TPB}	2.14×10^5	m^{-1}
Heat Conductivity		
λ_a	9.6	W m^{-1} K^{-1}
λ_c	6.23	W m^{-1} K^{-1}
λ_{el}	2.7	W m^{-1} K^{-1}
Heat Capacity		
$C_{p,a}$	420	J kg^{-1} K^{-1}
$C_{p,c}$	390	J kg^{-1} K^{-1}
$C_{p,el}$	300	J kg^{-1} K^{-1}
Density		
ρ_a	6570	kg m^{-3}
ρ_c	6870	kg m^{-3}
ρ_{el}	2000	kg m^{-3}

Here, E_{eq} is the equilibrium potential, η_{act} is the activation overpotential, and η_{ohmic} is the ohmic overpotential. The calculations of E_{eq} for the H_2-O_2 and CO-O_2 pairs are given in Eqs. (5) and (6), respectively.

$$E_{H_2} = E^0_{H_2} + \frac{RT}{2F} \ln\left[\frac{P^L_{H_2}\left(P^L_{O_2}\right)^{1/2}}{P^L_{H_2O}}\right] \tag{5}$$

$$E_{CO} = E^0_{CO} + \frac{RT}{2F} \ln\left[\frac{P^L_{CO}\left(P^L_{O_2}\right)^{1/2}}{P^L_{CO_2}}\right] \tag{6}$$

For numerical simplification, the value of the standard potentials ($E^0_{H_2}$ and E^0_{CO}) can be estimated using Eqs. (7) and (8) at high temperatures [27].

$$E^0_{H_2} = 1.253 - 0.00024516T(V) \tag{7}$$

$$E^0_{CO} = 1.46713 - 0.0004527T(V) \tag{8}$$

The Butler–Volmer (B-V) equation is adopted to calculate η_{act}, as given in Eq. (9).

$$i = i_0\left\{\exp\left(\frac{\alpha n F \eta_{act}}{RT}\right) - \exp\left(-\frac{(1-\alpha)nF\eta_{act}}{RT}\right)\right\} \tag{9}$$

Here, the exchange current density (i_0) of H_2 oxidation (as indicated in Eq. (2)) can be further expressed using Eq. (10), and the value of i_0 for Eq. (2) (H_2 oxidation) is expected to be 2.2-times that in Eq. (3) (CO oxidation) according to the experiments [26].

$$i_0 = \gamma \exp\left(-\frac{E_{act}}{RT}\right) \tag{10}$$

Here, γ is the pre-exponential factor, which builds an empirical relationship between the temperature and rate.

In addition, η_{ohmic}, caused by the ionic and electronic resistance, is calculated using Ohm's law, as given in Eqs. (11) and (12).

$$i_l = -\sigma_l^{eff}\nabla(\emptyset_l) \tag{11}$$

$$i_s = -\sigma_s^{eff}\nabla(\emptyset_s) \tag{12}$$

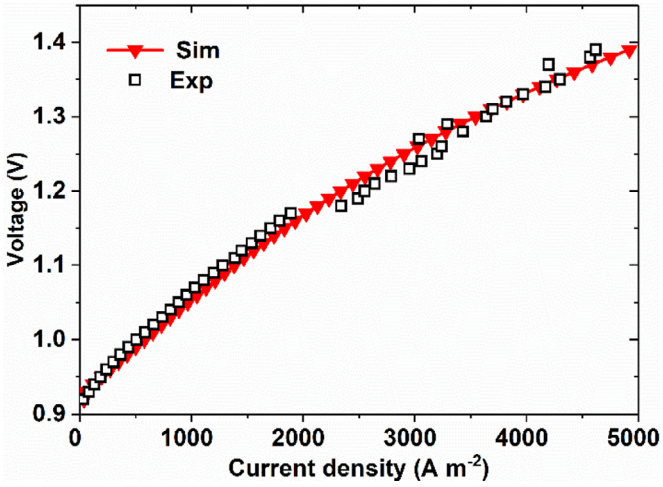

Fig. 2. Comparison of I–V characteristics between experimental data and simulation results.

2.2.2. Chemical reaction

Steam methane reforming (SMR) and water gas shift (WGS) reactions are considered at the anode, as given in Eqs. (13) and (14).

$$CH_4 + H_2O \leftrightarrow CO + 3H_2 \tag{13}$$

$$CO + H_2O \leftrightarrow CO_2 + H_2 \tag{14}$$

The detailed kinetics of SMR and WGS with a nickel catalyst can be found in [27–30].

2.2.3. Mass/momentum transport

In gas channels, only free molecule diffusion is considered to calculate the mass transport of a gas species. In the porous areas (such as a porous anode and cathode), the length of scale is comparable to the mean free path of the gas species. Therefore, the Knudsen diffusion is further included to calculate the mass transport of a gas species in a porous anode and cathode. Here, the widely used dusty-gas model is adopted to calculate the mass transport of the gas species ($N_{i/j}$), as indicated in

$$\frac{N_i}{D^{eff}_{ik}} + \sum_{j=1,\ j\neq i}^{n}\frac{y_jN_i - y_iN_j}{D^{eff}_{ij}} = -\frac{1}{RT}\left(\nabla(y_jP) + \frac{B_0y_jP}{\mu D^{eff}_{ik}}\nabla P\right) \tag{15}$$

When operating under a steady state with the mass source term (S_j), the mass conservation equation is calculated using

$$\nabla \cdot N_j = S_j \tag{16}$$

The Navier–Stokes equation is adopted to calculate the momentum transport, as given in Eq. (17).

$$\rho\frac{\partial u}{\partial t} + \rho u\nabla u = -\nabla p + \nabla\left[\mu\left(\nabla u + (\nabla u)^T\right) - \frac{2}{3}\mu\nabla u\right] - \frac{\varepsilon\mu u}{k} \tag{17}$$

Here, u is the velocity field, μ is the dynamic viscosity of the fluid, and k is the permeability of a porous area.

2.2.4. Heat transfer

The heat balance equation is used to describe the heat transfer process, as given in Eq. (18).

$$\rho C_p u\cdot\nabla T + \nabla\cdot\left(-\lambda_{eff}\nabla T\right) = Q \tag{18}$$

Here, ρ is the fluid density, C_p is the heat capacity, and Q is the heat source term.

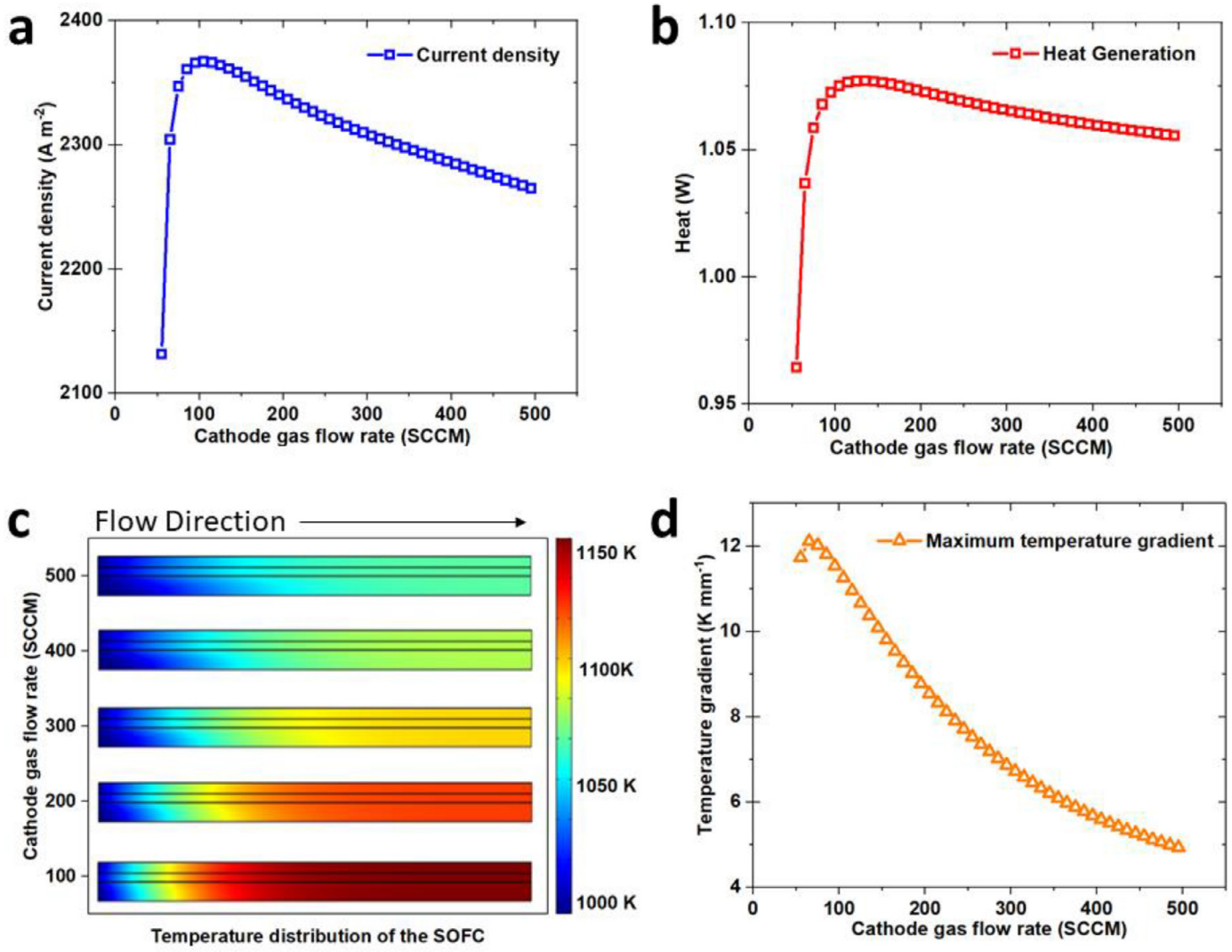

Fig. 3. Effects of the gas flow rate of the cathode inlet on the SOFC performance.

2.2.5. *Validation of multi-physics simulation*

For validation, the model adopts the same operating conditions, cell geometry, and material properties in accordance with the experiments [26], and the I–V relationships from the simulation and experiment are compared at an operating temperature of 1073 K, as indicated in Fig. 2 [31]. The detailed material properties and reaction parameters used in the model are provided in Tables 1 and 2.

2.3. *Combination of MPS model with deep learning (DL) algorithm*

Although an MPS can provide useful information for analysis and optimisation, such simulations are too complex for model-based online control systems. Compared with MPS models, a BBM can be constructed without physical laws, making it swift in mapping the inputs to the outputs. A BBM based on the DL algorithm has been widely used for nonlinear systems with multiple inputs and outputs, and is thus suitable for predicting the performance of SOFCs.

A DNN is a statistical data-driven approach inspired by biological neural networks. Given proper input-output pairs, it can capture the functional relationship without presumptions. It usually has a computational topology consisting of one input layer, multiple hidden layers, and one output layer. Each layer has several processing units (neurons). These neurons receive multiple inputs (information) from other neurons with certain connection weights. The information is summated and transformed with an activation function to produce the output, which is propagated to other neurons in the next layer.

Because the MPS model can easily provide a sufficiently large database required for the training of the DNN algorithm, the combi-

Table 2
Kinetics and tuning parameters.

Parameters	Value or expression	Unit
Electrochemical Reaction		
β	3.3×10^8	Am^{-2}
E_a	1.2×10^5	J mol^{-1}
α_{H_2O}	0.65	
α_{CO_2}	0.65	
Chemical Reaction		
R_{MSR} [33]	$k_{rf}(p_{CH_4}p_{H_2O} - \frac{p_{H_2}^3 p_{CO}}{K_{pr}})$	mol m^{-3} s^{-1}
k_{rf}	$2395\exp(\frac{-231,266}{RT})$	mol m^{-3} Pa^{-2} s^{-1}
K_{pr}	$1.0267 \times 10^{10}\exp(-0.2513Z^4 + 0.3665Z^3 + 0.5810Z^2 - 27.134Z + 3.277)$	
R_{WGSR} [34]	$k_{sf}(p_{H_2O}p_{CO} - \frac{p_{H_2}p_{CO_2}}{K_{ps}})$	mol m^{-3} s^{-1}
k_{sf}	$0.0171\exp(\frac{-103,191}{RT})$	mol m^{-3} Pa^{-2} s^{-1}
K_{ps}	$\exp(-0.2935Z^3 + 0.6351Z^2 + 4.1788Z + 0.3169)$	
Z	$\frac{1000}{T} - 1$	

Table 3
Operating parameters for studying the effects of the gas flow rate of the cathode inlet.

Parameter	Value	Unit
Anode gas flow rate	10	SCCM
Cathode gas flow rate	50–500	SCCM
Anode gas composition	H_2 (60%) + CO (25%) + CH_4 (3%) + H_2O (6%) + CO_2 (6%)	
Cathode gas composition	Air (O_2, 21% + N_2, 79%)	
Anode inlet temperature	973	K
Cathode inlet temperature	973	K
Applied voltage	0.7	V

Table 4
Operating parameters for studying the effects of the gas temperature of the cathode inlet.

Parameter	Value	Unit
Anode gas flow rate	10	SCCM
Cathode gas flow rate	500	SCCM
Anode gas composition	H_2 (60%) + CO (25%) + CH_4 (3%) + H_2O (6%) + CO_2 (6%)	
Cathode gas composition	Air (O_2, 21% + N_2, 79%)	
Anode inlet temperature	973	K
Cathode inlet temperature	773–973	K
Applied voltage	0.7	V

Table 5
Operating parameters for studying the effects of the gas flow rate of the anode inlet.

Parameter	Value	Unit
Anode gas flow rate	12, 14, 16, 18, 20	SCCM
Cathode gas flow rate	500	SCCM
Anode gas composition	H_2 (60%) + CO (25%) + CH_4 (3%) + H_2O (6%) + CO_2 (6%)	
Cathode gas composition	Air (O_2, 21% + N_2, 79%)	
Anode inlet temperature	973	K
Cathode inlet temperature	973	K
Applied voltage	0.7	V

Table 6
Operating parameters for comparison of the DNN and MPS results.

Parameter	Value	Unit
Anode gas flow rate	15	SCCM
Cathode gas flow rate	200, 300, 400, 500	SCCM
Anode gas composition	H_2 (60%) + CO (25%) + CH_4 (3%) + H_2O (6%) + CO_2 (6%)	
Cathode gas composition	Air (O_2, 21% + N_2, 79%)	
Anode inlet temperature	973	K
Cathode inlet temperature	973	K
Applied voltage	0.7	V

nation of an MPS and a DNN not only avoids the expensive costs and time needed during the experiments but also provides a precise and fast tool for analysing the SOFC operation.

In this study, a three-hidden-layer back-propagation DNN (BP-DNN) (as shown in Fig. 1) is adopted with eight inputs and three outputs. The inputs are characteristic parameters that significantly affect the cell performance and can be detected during an online operation, i.e. the current density, anode flow rate, cathode flow rate, and temperatures at five points evenly distributed along the cell length from the inlet to the outlet. The outputs are the parameters that reflect the efficiency and thermal behaviour of the cell but are difficult to measure during an online operation, i.e. the generated heat and maximum temperature gradient along the cell length and membrane assembly directions. A $17{,}384 \times 11$ data matrix is split into two sets with a ratio of 0.8:0.2, the former of which is used for DNN training and the latter for testing. The epoch and batch sizes are set to 8000 and 200, respectively. The training accuracy of the DNN model reaches 99.9%, which is sufficiently high for further prediction.

Based on the trained DNN model, a GA was adopted for online optimisation, as shown in Fig. 1. The key parameters of the GA are the number of evaluated solutions in every iteration (population), the number of iterations (generation), the frequency of merging feature (crossover rate), the frequency of random changes (mutation), and the number of solutions (tournament size), the values of which are 100, 100, 0.8, 0.2, and 4, respectively.

3. Results and discussion

As the key performance parameters, the power density, energy efficiency, and thermal behaviour are evaluated by studying the effects of the operating conditions on the current density (at a given voltage), heat generation, temperature distribution (including the channel area), and maximum temperature gradient. The flow rate and temperature at the cathode inlet, and the flow rate at the anode, are the adjustable operating parameters applied herein. The detailed operating conditions described in Sections 3.1–3.5 are listed in Tables 3–6.

3.1. Effects of flow rate at cathode

The flow rate at the cathode is found to significantly affect the temperature distribution of the SOFC within the full range, as shown in Fig. 3. At low flow rates (<100 SCCM), the increase in the flow rate at the cathode improves the current density owing to the need for an O_2 supply during the electrochemical reactions. With a further increase in the flow rate, more heat generated from the inner reactions is taken away by the gas flow, resulting in a decrease in the reaction kinetics and heat generation, therefore decreasing the current density. With an increase in the flow rate of the cathode from 105 to 495 SCCM, a more uniform temperature distribution is observed, where a 59.3% decrease in the maximum temperature gradient is found (from 11.25 to 4.93 K mm^{-1}), with only a 3.4% and 2.0% decrease in the current density and heat generation, respectively.

3.2. Effects of temperature at cathode inlet

The gas temperature at the cathode inlet was found to significantly affect the current density, heat generation, and temperature distribution of the SOFCs within the entire range, as shown in Fig. 4. With a decrease in the gas temperature of the cathode inlet from 970 to 770 K, the current density, heat generation, and maximum temperature gradient in the cell length direction were found to decrease by 48.7% (from 2251 to 1155 A m^{-2}), 40.4% (from 1.05 to 0.63 W), and 73.2% (from 4.70 to 1.26 K mm^{-1}), respectively. However, the large temperature gradient along the cell assembly direction should be noted under low-temperature conditions, which may cause a cell failure. Moreover, the SOFC shows different behaviours of the maximum temperature gradient at two regimes with an increase in the inlet gas temperature of the cathode. This behaviour is related with the change in area where the maximum temperature gradient appears. Within the low inlet temperature regime of the cathode, the maximum temperature gradient appears in an area close to the cathode inlet owing to the difference in the inlet gas temperatures at the two electrodes. At high gas temperatures of the cathode inlet, however, the maximum temperature gradient appears in the area close to the anode inlet owing to the significant heat generation from electrochemical reactions.

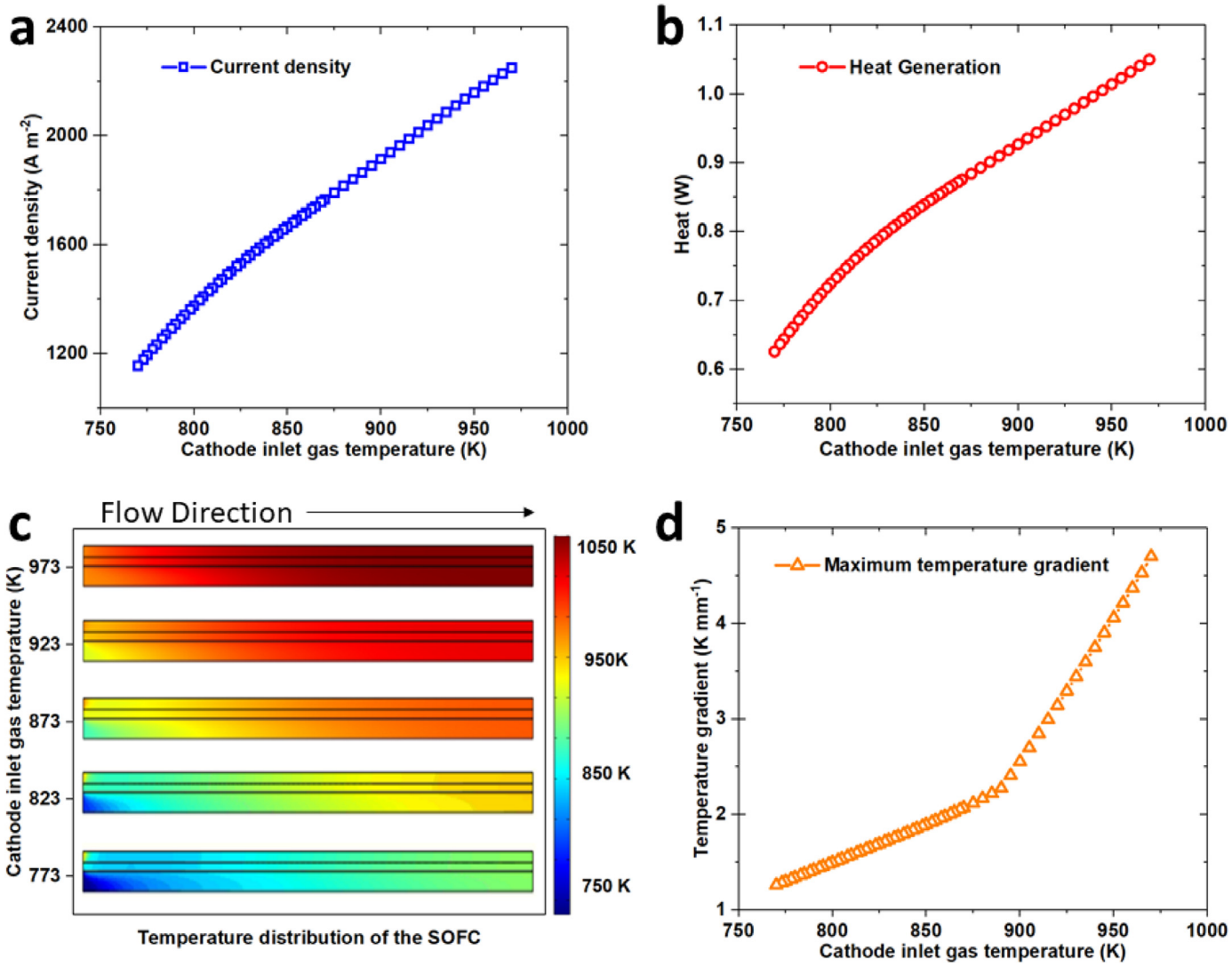

Fig. 4. Effects of the gas temperature of the cathode inlet on the SOFC performance.

3.3. Effects of flow rate at anode

The effects of the anode flow rate on the cell performance at different inlet gas temperatures at the cathode are given in Fig. 5. Larger increases in the current density and heat are found at higher operating temperatures, where both the current density and heat increase by 31.8% at a high gas temperature (973 K) of the cathode inlet with the anode flow rate increasing from 12 to 20 SCCM. At a low temperature (773 K) of the cathode inlet, the increase in the current density and heat generation is only 20.6% and 23.2%, respectively. By contrast, the increase in the anode gas flow rate has a larger effect on the maximum temperature gradient at a lower gas temperature of the cathode inlet, where the increases at inlet temperatures of 773 and 973 K are 23.0% and 7.2%, respectively.

3.4. Prediction of maximum temperature gradient

The accuracy of the maximum temperature gradient predicted by the DNN model was evaluated by comparing it with the results of the MPS model at different gas flow rates of the cathode inlet. The relative error (*Re*) is defined as $Re = (\text{DNN}/\text{MPS-1}) \times 100\%$. As shown in Fig. 6, the relative errors are within the ranges of −1.22%–1.10%, −1.56%–2.32%, −2.24%–1.42%, and −6.12%–0.05% with the gas flow rate at the cathode inlet being 200, 300, 400, and 500 SCCM, respectively. The absolute average relative errors in these four groups are respectively 0.54%, 1.05%, 1.00%, and 1.11%. The low relative error range and absolute average error value prove the precision of the DNN model in predicting the maximum temperature gradient in the SOFC at different gas flow rates of the cathode inlet. In addition, Fig. 6 shows the importance of increasing the cathode flow rate in decreasing the maximum temperature gradient in the SOFCs. With the flow rate of the cathode increasing from 200 to 500 SCCM, the maximum temperature gradient decreases from 9.33 to 4.98 K mm^{-1} (a 46.6% decrease) and from 6.40 to 1.43 K mm^{-1} (a 77.7% decrease) at 973 and 773 K, respectively.

3.5. Prediction of heat generation

Compared with the low errors when using the DNN model to predict the maximum temperature gradient, even lower errors are found when using the model to predict the heating generation in the SOFCs. As shown in Fig. 7, the relative errors are within the ranges of 0.36%–3.94%, −0.61%–1.48%, −0.88%–0.73%, and −0.83%–2.75% with a gas flow rate of the cathode inlet of 200, 300, 400, and 500 SCCM, respectively. The absolute average relative errors in these four groups are 0.92%, 0.47%, 0.44%, and 0.87%. The relative error ranges are lower than 3.58% and the absolute average error is only 0.68%, proving the precision of the DNN model in predicting the heat generation in the SOFCs at different gas flow rates of the cathode inlet. In addition, it was

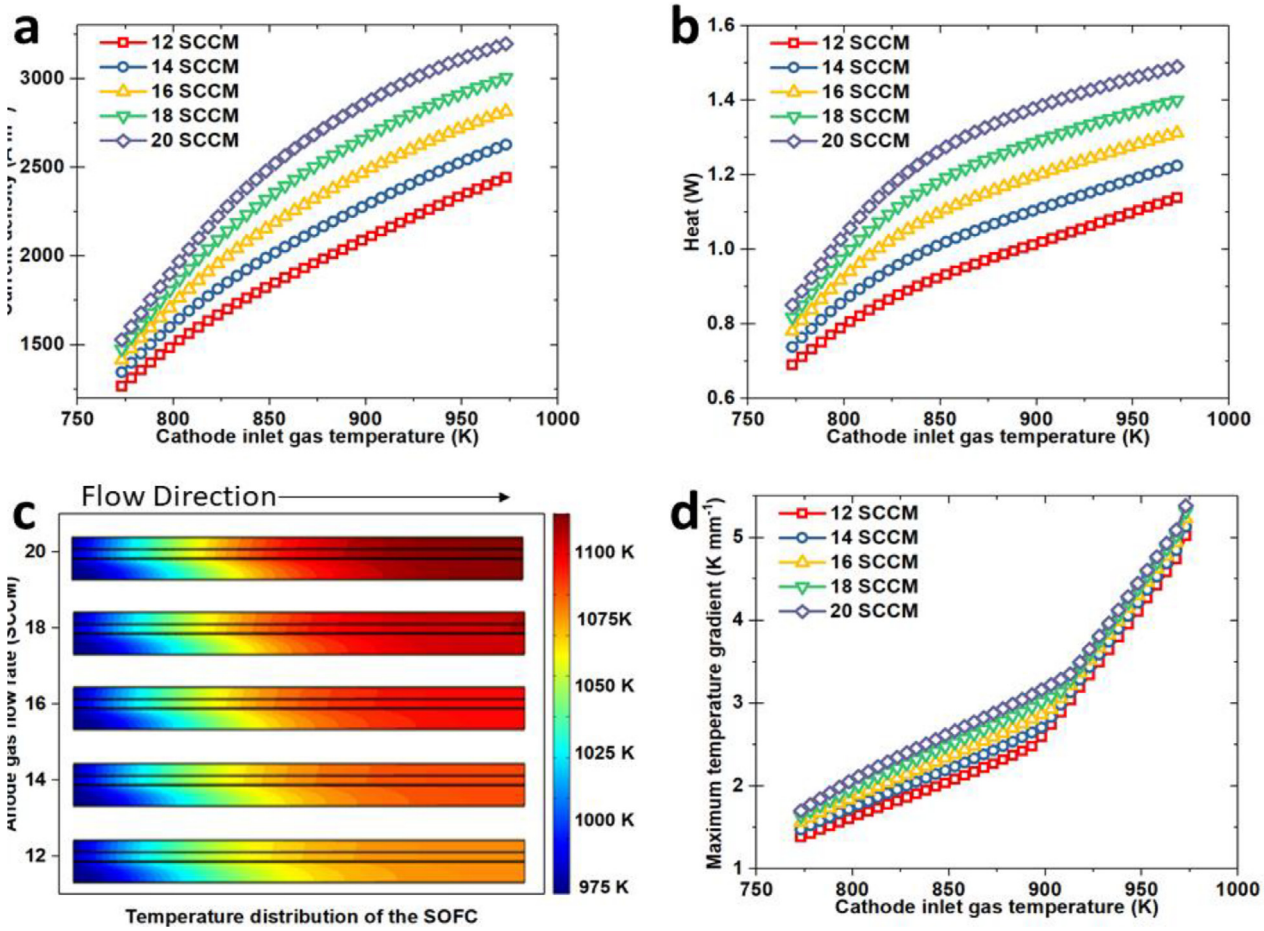

Fig. 5. Effects of the gas flow rate of the anode inlet on the SOFC performance.

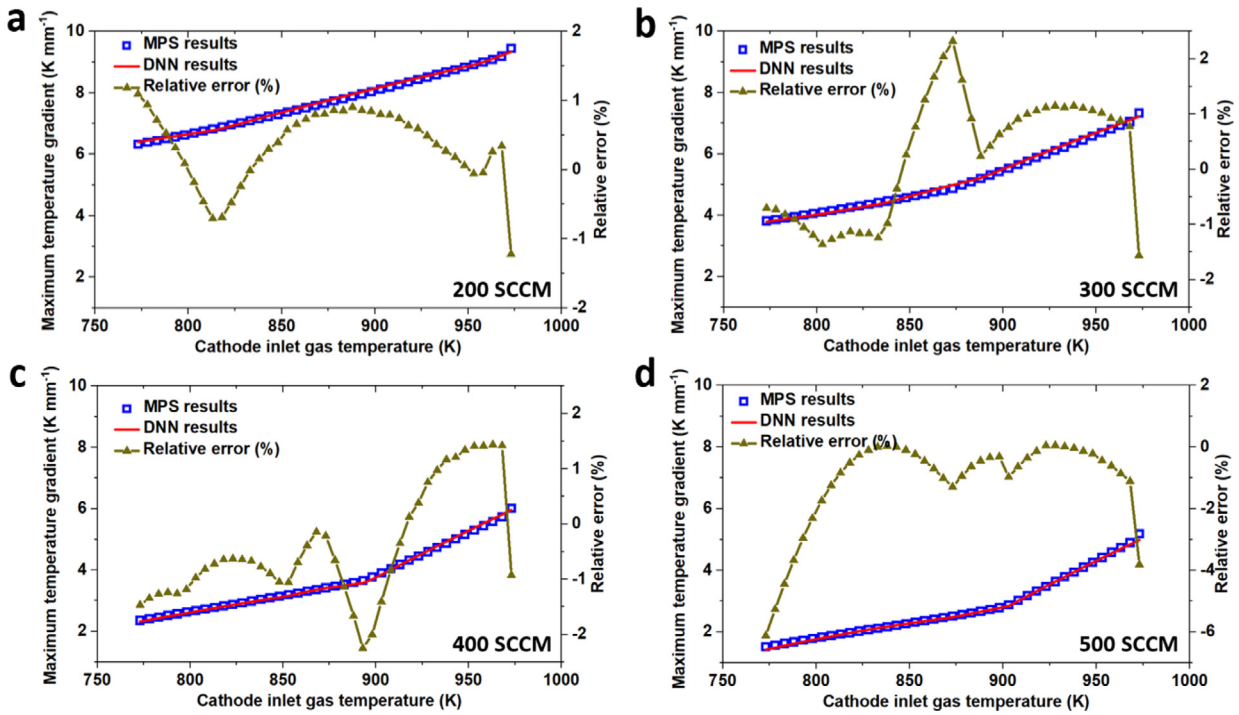

Fig. 6. Comparison of the MPS and DNN models in the prediction of the maximum temperature gradient in SOFCs at different gas flow rates of the cathode inlet.

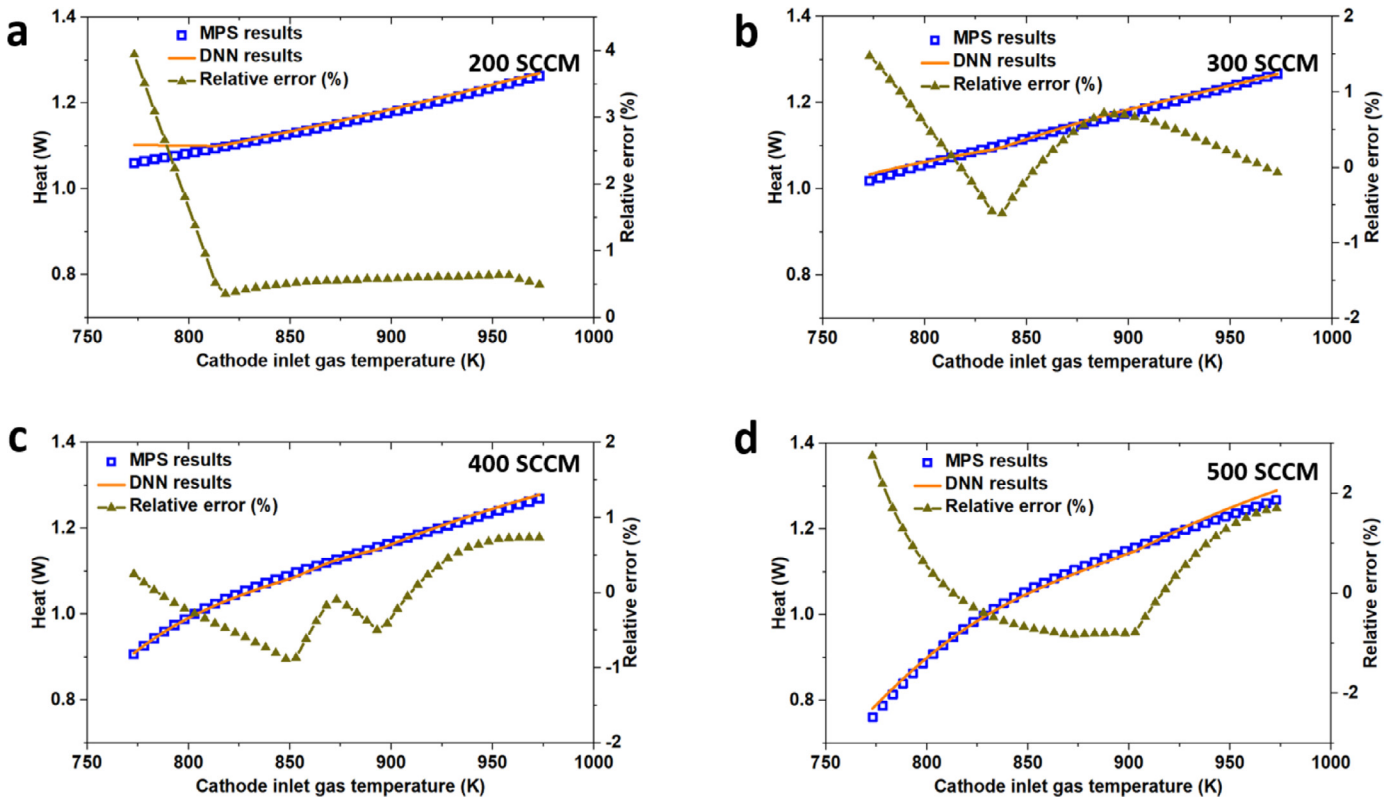

Fig. 7. Comparison of the MPS and DNN models in the prediction of the heat generation in SOFCs at different gas flow rates of the cathode inlet.

Table 7
Operating parameters for the optimisation using genetic algorithm.

Parameter	Value	Unit
Anode gas flow rate	10–20	SCCM
Cathode gas flow rate	100–500	SCCM
Anode gas composition	H_2 (60%) + CO (25%) + CH_4 (3%) + H_2O (6%) + CO_2 (6%)	
Cathode gas composition	Air (O_2, 21% + N_2, 79%)	
Anode inlet temperature	973	K
Cathode inlet temperature	773–973	K
Applied voltage	0.7	V

found that the heat generated is significantly decreased with a low gas temperature and high gas flow rate of the cathode inlet.

3.6. Optimisation procedure using the genetic algorithm

GA is the most popular type of evolutionary algorithm inspired by biological evolution, and seeks a solution in the form of strings of binary digits (representing chromosomes), which generate offspring through selection, crossover, and mutation. These candidates are evaluated using a fitness function, where the iteration continues until the convergence criterion is met. As a heuristic method, GA is suitable for optimisation problems provided a proper database is used.

The optimisation procedure of the GA is conducted based on the well-trained DNN algorithm. The maximum output power density is set as the target parameter for different gas flow rates of the anode (10–20 SCCM). Meanwhile, the temperature gradient limitation is set to <2 K mm^{-1} considering the thermal safety, and the operating conditions of the flow rate and gas temperature of the cathode inlet are set to lower than 500 SCCM and 973 K, respectively. The operating conditions are given in Table 7.

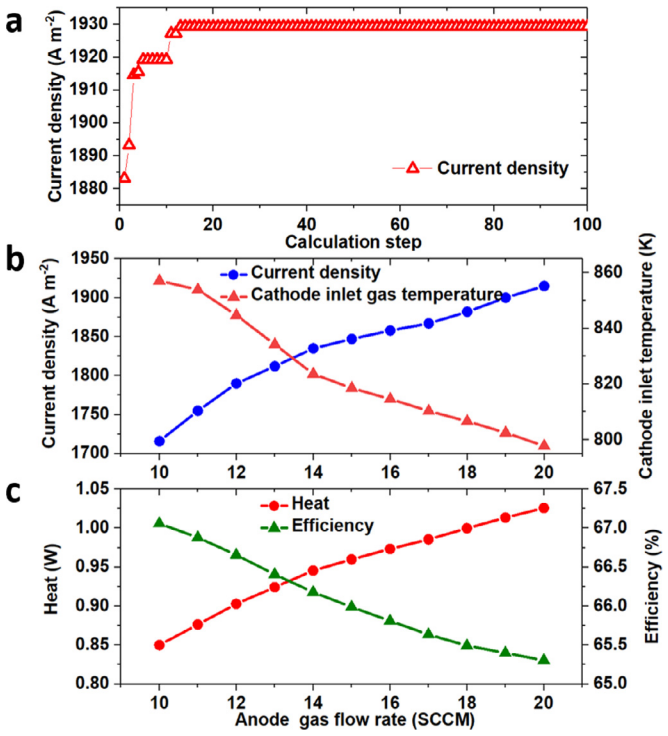

Fig. 8. (a) Calculation steps for the independent validation of the optimisation procedure using a genetic algorithm within the temperature gradient limitation and parameter range of the operating conditions, (b) optimised current density and cathode inlet temperature at the maximum power density target, and (c) the value of the heat and fuel efficiency under optimised operating conditions.

The validation of the calculation step independence of the GA for optimisation is shown in Fig. 8a. The optimisation results after 100 steps are adopted, where the convergence is achieved within 20 steps. Fig. 8b simulates the real-time change of the gas flow rate of the anode inlet during a practical operation, where the flow rate fluctuates between 10 and 20 SCCM. As analysed previously, small fluctuations of the flow rate at the anode cause a large change in the heat generation and a temperature gradient, which decreases the efficiency and damages the SOFCs. With the optimisation of the GA, the gas temperature of the cathode inlet declines in accordance with the increase in the gas flow rate of the anode inlet. As a result, the operating current density increases to a higher level, and the temperature gradient is controlled within the threshold. Under the optimised operating conditions, the generated heat and related fuel efficiency, defined as

$$\text{Efficiency} = \frac{\text{Electricity}}{\text{Electricity} + \text{Heat}}, \tag{19}$$

change with an increase in the gas flow rate of the anode, as shown in Fig. 8c. An increase in the heat generation is observed from 0.85 to 1.03 W with the flow rate of the anode increasing from 10 to 20 SCCM. Compared with a 21% increase in the heat generation, the decrease in efficiency is only 1.8% owing to the 12% increase in electricity generation. The fuel efficiency remains at above 65% under the studied operating conditions, showing the advantage of the optimisation algorithm.

4. Conclusion

A hybrid method combining an MPS and deep learning was developed to predict the key characteristics of SOFCs operating with a complex fuel composition. The DNN algorithm was trained using a dataset generated from the verified MPS model, in which the electrochemical reactions, chemical reactions, mass/momentum transport (CFD), and heat transfer were fully considered. The maximum temperature gradient and heat generation in the SOFCs were predicted using the trained DNN algorithm under different operating conditions, including the current density, inlet gas flow rate, and inlet gas temperature. The preliminary simulation results show the high accuracy of a DNN prediction, where the absolute average relative errors in predicting the average maximum temperature gradient and heat generation are only 0.975% and 0.68%, respectively.

To achieve a closed cycle from detection to analysis and optimisation, the real-time fluctuations of the gas flow rate at the anode inlet were simulated. Through a GA optimisation, the maximum-output-power-density target was achieved at different gas flow rates of the anode by analysing the combination of different operating parameters. The maximum temperature gradient of the cell was set as the threshold to ensure the safe operation of the SOFCs under different operating conditions. Finally, a high fuel efficiency (> 65%) was maintained through the optimisation procedure.

The combination of an MPS, a DNN, and a GA provides a promising solution for model-based control systems for precisely and quickly analysing the performances of SOFCs and other non-linear systems. Currently, the deep learning algorithm trained in this study is based only on simulation data under stationary operating conditions. Further training with more experimental data on the algorithm is needed for a wider application under dynamic operating conditions.

Code availability

The Keras package is available from [32]. The code for the DNN training, prediction, and GA optimisation are available at https://github.com/Ma-Jingbo/MPS-AI-Haoran-Xu.

Declaration of Competing Interest

The authors declare that they have no known competing financial interests or personal relationships that could have appeared to influence the work reported in this paper.

Acknowledgement

M. Ni would like to thank the Research Grant Council, University Grant Committee, Hong Kong SAR for the grant provided (Project nos. PolyU 152214/17E and PolyU 152064/18E). J Xuan would like to acknowledge the funding support from the Royal Society through Grant no. NAF\R1\180146. P. Tan would like to thank the CAS Pioneer Hundred Talents Program (KJ 2090130001), USTC Research Funds of the Double First-Class Initiative (YD 2090002006), and USTC Tang Scholar for providing the funding support. Y. Zhang gratefully acknowledges the financial support from the Natural Science Foundation of China (21673062).

References

[1] Glenk G, Reichelstein S. Economics of converting renewable power to hydrogen. Nat Energy 2019;4:216–22. doi:10.1038/s41560-019-0326-1.
[2] Lewis NS. Research opportunities to advance solar energy utilization. Science 2016(80):351. doi:10.1126/science.aad1920.
[3] Ormerod RM. Solid oxide fuel cells. Chem Soc Rev 2003;32:17–28. doi:10.1039/B105764M.
[4] Mahato N, Banerjee A, Gupta A, Omar S, Balani K. Progress in material selection for solid oxide fuel cell technology: a review. Prog Mater Sci 2015;72:141–337. doi:10.1016/j.pmatsci.2015.01.001.
[5] Singhal SC. Advances in solid oxide fuel cell technology. Solid State Ionics 2000;135:305–13. doi:10.1016/S0167-2738(00)00452-5.
[6] Xu H, Chen B, Liu J, Ni M. Modeling of direct carbon solid oxide fuel cell for CO and electricity cogeneration. Appl Energy 2016;178:353–62. doi:10.1016/j.apenergy.2016.06.064.
[7] Gür TMM. Comprehensive review of methane conversion in solid oxide fuel cells: prospects for efficient electricity generation from natural gas. Prog Energy Combust Sci 2016;54:1–64. doi:10.1016/j.pecs.2015.10.004.
[8] Jiao Y, Zhao J, An W, Zhang L, Sha Y, Yang G, et al. Structurally modified coal char as a fuel for solid oxide-based carbon fuel cells with improved performance. J Power Sources 2015;288:106–14. doi:10.1016/j.jpowsour.2015.04.121.
[9] Alexander BR, Mitchell RE, Gür TM. Experimental and modeling study of biomass conversion in a solid carbon fuel cell. J Electrochem Soc 2012;159:B347–54. doi:10.1149/2.096203jes.
[10] Perna A, Minutillo M, Jannelli E, Cigolotti V, Nam SW, Han J. Design and performance assessment of a combined heat, hydrogen and power (CHHP) system based on ammonia-fueled SOFC. Appl Energy 2018;231:1216–29. doi:10.1016/j.apenergy.2018.09.138.
[11] Chen Y, deGlee B, Tang Y, Wang Z, Zhao B, Wei Y, et al. A robust fuel cell operated on nearly dry methane at 500°C enabled by synergistic thermal catalysis and electrocatalysis. Nat Energy 2018;3:1042–50. doi:10.1038/s41560-018-0262-5.
[12] Sharma M, Rakesh N, Dasappa S. Solid oxide fuel cell operating with biomass derived producer gas: status and challenges. Renew Sustain Energy Rev 2016;60:450–63. doi:10.1016/j.rser.2016.01.075.
[13] Xu H, Chen B, Tan P, Cai W, He W, Farrusseng D, et al. Modeling of all porous solid oxide fuel cells. Appl Energy 2018;219:105–13. doi:10.1016/j.apenergy.2018.03.037.
[14] de Avila Ferreira T, Wuillemin Z, Marchetti AG, Salzmann C, Van Herle J, Bonvin D. Real-time optimization of an experimental solid-oxide fuel-cell system. J Power Sources 2019;429:168–79. doi:10.1016/j.jpowsour.2019.03.025.
[15] Xu H, Chen B, Zhang H, Sun Q, Yang G, Ni M. Modeling of direct carbon solid oxide fuel cells with H_2O and CO_2as gasification agents. Int J Hydrogen Energy 2017;42:15641–51. doi:10.1016/j.ijhydene.2017.05.075.
[16] Li W, Shi Y, Luo Y, Cai N. Elementary reaction modeling of CO_2/H_2O co-electrolysis cell considering effects of cathode thickness. J Power Sources 2013;243:118–30. doi:10.1016/j.jpowsour.2013.05.119.
[17] Lu X, Li T, Bertei A, Cho JIS, Heenan TMM, Rabuni MF, et al. The application of hierarchical structures in energy devices: new insights into the design of solid oxide fuel cells with enhanced mass transport. Energy Environ Sci 2018;11:2390–403. doi:10.1039/C8EE01064A.
[18] Bove R, Lunghi P, Sammes NM. SOFC mathematic model for systems simulations. Part one: from a micro-detailed to macro-black-box model. Int J Hydrogen Energy 2005;30:181–7. doi:10.1016/j.ijhydene.2004.04.008.
[19] Wang B, Xie B, Xuan J, Jiao K. AI-based optimization of PEM fuel cell catalyst layers for maximum power density via data-driven surrogate modeling. Energy Convers Manag 2020;205:112460. doi:10.1016/j.enconman.2019.112460.
[20] Bejan A. AI and freedom for evolution in energy science. Energy AI 2020:100001. doi:10.1016/j.egyai.2020.100001.
[21] Rudin C. Stop explaining black box machine learning models for high stakes decisions and use interpretable models instead. Nat Mach Intell 2019;1:206–15. doi:10.1038/s42256-019-0048-x.

[22] Arriagada J, Olausson P, Selimovic A. Artificial neural network simulator for SOFC performance prediction. J Power Sources 2002;112:54–60. doi:10.1016/S0378-7753(02)00314-2.
[23] Perc M, Ozer M, Hojnik J. Social and juristic challenges of artificial intelligence. Palgrave Commun 2019;5:61. doi:10.1057/s41599-019-0278-x.
[24] Yan Z, He A, Hara S, Shikazono N. Modeling of solid oxide fuel cell (SOFC) electrodes from fabrication to operation: microstructure optimization via artificial neural networks and multi-objective genetic algorithms. Energy Convers Manag 2019;198:111916. doi:10.1016/j.enconman.2019.111916.
[25] Vo ND, Oh DH, Hong S-H, Oh M, Lee C-H. Combined approach using mathematical modelling and artificial neural network for chemical industries: steam methane reformer. Appl Energy 2019;255:113809. doi:10.1016/j.apenergy.2019.113809.
[26] Luo Y, Shi Y, Li W, Cai N. Comprehensive modeling of tubular solid oxide electrolysis cell for co-electrolysis of steam and carbon dioxide. Energy 2014;70:420–34. doi:10.1016/j.energy.2014.04.019.
[27] Ni M. Modeling and parametric simulations of solid oxide fuel cells with methane carbon dioxide reforming. Energy Convers Manag 2013;70:116–29. doi:10.1016/j.enconman.2013.02.008.
[28] Wang Y, Yoshiba F, Kawase M, Watanabe T. Performance and effective kinetic models of methane steam reforming over Ni/YSZ anode of planar SOFC. Int J Hydrogen Energy 2009;34:3885–93. doi:10.1016/j.ijhydene.2009.02.073.
[29] Luo Y, Li W, Shi Y, Cao T, Ye X, Wang S, et al. Experimental characterization and theoretical modeling of methane production by H_2O/CO_2 co-electrolysis in a tubular solid oxide electrolysis cell. J Electrochem Soc 2015;162:F1129–34. doi:10.1149/2.0171510jes.
[30] Ni M, Leung DYC, Leung MKH. Electrochemical modeling and parametric study of methane fed solid oxide fuel cells. Energy Convers Manag 2009;50:268–78. doi:10.1016/j.enconman.2008.09.028.
[31] Xu H, Chen B, Irvine J, Ni M. Modeling of CH 4 -assisted SOEC for H_2O/CO_2 co-electrolysis. Int J Hydrogen Energy 2016;41:21839–49. doi:10.1016/j.ijhydene.2016.10.026.
[32] Chollet, F. (2015) keras, GitHub. https://github.com/fchollet/keras.
[33] Ni M. 2D heat and mass transfer modeling of methane steam reforming for hydrogen production in a compact reformer. Energy Convers Manag 2013;65:155–63. doi:10.1016/j.enconman.2012.07.017.
[34] Ni M. An electrochemical model for syngas production by co-electrolysis of H_2O and CO_2. J Power Sources 2012;202:209–16. doi:10.1016/j.jpowsour.2011.11.080.